Available online at www.sciencedirect.com
SCIENCE DIRECT®
International Journal of Heat and Mass Transfer 49 (2006) 4454–4468
International Journal of HEAT and MASS TRANSFER
www.elsevier.com/locate/ijhmt

Modeling of coupled spectral radiation, thermal and carrier transport in a silicon photovoltaic cell

Rodolphe Vaillon *, Lucile Robin, Cristian Muresan, Christophe Ménézo

Centre de Thermique de Lyon (CETHIL, CNRS-INSA Lyon-UCBL), Bât. Sadi Carnot, INSA de Lyon, 20 av. A. Einstein, 69621 Villeurbanne Cedex, France

Received 6 December 2005; received in revised form 25 April 2006
Available online 12 July 2006

Abstract

Photovoltaic conversion efficiency of a crystalline silicon cell is investigated as a function of its temperature and taking into account complete thermal and irradiation operating conditions. The spectral radiative transfer problem is solved through a gray per band approach and a separated treatment of the collimated and diffuse components of radiation fluxes. The heat transfer modeling includes local heat sources due to radiation absorption and thermal emission, non-radiative recombinations and excess power release of photo-generated carriers. Continuity equations for minority carriers are solved to provide the current–voltage characteristic. A detailed analysis of the electrical and thermal behaviors demonstrates that proper adjustment and control of both thermal and surroundings radiative operating conditions are likely to provide guidelines for the improvement of photovoltaic cell performances.
© 2006 Elsevier Ltd. All rights reserved.

Keywords: Radiative–conductive heat transfer; Photoelectric conversion; Silicon photovoltaic solar cells

1. Introduction

Photovoltaic cells are being employed for plenty of applications consisting in electricity supply to systems such as remote area devices, space satellites, solar powered engines. Recent years have given rise to an increase of photovoltaic cell use for a better and intensive benefit of the renewable solar energy. As an example, integration of solar panels to buildings is likely to participate significantly to the overall electricity production in future decades.

In this context, research on photovoltaic cells still has to be conducted to bring solutions for the improvement of their performances. Among several objectives such as semiconductor material choice and best processing to achieve optimal properties, this paper focuses on the electrical performances of silicon solar cells as a function of its temperature, which itself results from thermal and irradiation conditions. A recent review of Radizemska [1] on the performances of Si and GaAs solar cells exhibits the main parameters and phenomena which affect their output, with a focus on specific photovoltaic-thermal and building integrated PV systems (BiPV). It is concluded that absorbed solar radiation that is not converted into electricity is one cause of cell temperature increase leading to an electrical efficiency decrease. To remedy this problem, proper ways to extract heat by forced or natural fluid circulation have to be determined. It is worth noticing that the heated fluid (air or/and water) may be also used for buildings needs. As a consequence, an accurate understanding of both the thermal and electrical behaviors of photovoltaic modules is required so as to find out best solutions for heat removal in connection with the cell design for best photovoltaic conversion efficiency.

Global heat transfer models have been proposed in previous investigations (see for example Refs. [2–7]) but they do not include a detailed description of the coupling between spectral radiative, thermal and electric carrier

* Corresponding author. Tel.: +33 4 72 43 88 17; fax: +33 4 72 43 88 11.
E-mail address: rodolphe.vaillon@insa-lyon.fr (R. Vaillon).

0017-9310/$ - see front matter © 2006 Elsevier Ltd. All rights reserved.
doi:10.1016/j.ijheatmasstransfer.2006.05.014

Nomenclature

c_0	speed of light in vacuum, $c_0 = 2.998 \times 10^8$ m s^{-1}
D	minority carrier diffusion coefficient (m^2 s^{-1})
E	electric field (V m^{-1})
E_g	band gap (eV)
E_p	phonon energy (eV)
G	incident radiation power (W m^{-2})
$g_{op,\Delta\nu}$	rate of minority carriers optically generated on the frequency interval $\Delta\nu$ (m^{-3} s^{-1})
h	Planck constant, $h = 6.6260693 \times 10^{-34}$ J s
h_f	convective heat transfer coefficient (W m^{-2} K^{-1})
I_ν	spectral radiation intensity (W m^{-2} sr^{-1} Hz^{-1})
J	current density (A m^{-2})
k	Boltzmann constant, $k = 1.3806505 \times 10^{-23}$ J K^{-1}
k_c	thermal conductivity (W m^{-1} K^{-1})
M	number of discrete layers
n	real part of the complex refractive index
n_e, n_h	carrier (electron, hole) density (cm^{-3})
n_i	intrinsic carrier density (cm^{-3})
N_a	acceptor density (cm^{-3})
N_d	donor density (cm^{-3})
q	total radiation flux (W m^{-2})
Q	total heat source (W m^{-3})
S	surface recombination velocity (m s^{-1})
T	temperature (K)
V_0	built-in voltage (V)
V	voltage (V)
w	thickness (m)

Greek symbols

κ	absorption coefficient (m^{-1})
λ_0	wavelength in vacuum (μm)
ν	frequency (Hz)
$\Delta\nu$	frequency interval (Hz)
τ	minority carrier lifetime (s)

Subscripts

0	dark equilibrium configuration
1	top side of the layer
2	bottom side of the layer
c	collimated component of radiation
d	diffuse component of radiation
dz	depletion zone
e	electrons
h	holes
f	surrounding fluid
i	intrinsic
inc	incident radiation
N	N-region
P	P-region
interband	related to the interband absorption process
fc	related to free carriers
latt	related to the lattice
solar	solar irradiation
oc	open circuit
sc	short circuit

transport. The objective of this work is to provide a physical and numerical model for the evaluation of photovoltaic cell performances as a function of its temperature considering thermal, solar and surroundings irradiations operating conditions.

Photovoltaic cells are encapsulated inside layers of glass and resin so as to form a module. However, for the sake of simplicity, a single P–N junction layer is considered. Section 2 is devoted to the theoretical formulation of the heat, spectral radiative and carrier transport problems. Although the physical modeling is quite adaptable to several types of semiconductor junctions, evaluation of required optical, radiative and thermophysical properties is given for the case of crystalline silicon cells, which are the most widespread ones. Numerical solution methods are explained in Section 3. As for applications, an analysis is carried out in Section 4. For this sake, the junction layer parameters and a set of configurations for spectral radiative and thermal boundary conditions are selected. The consistency of the numerical model for radiation heat transfer is first assessed by checking the radiation power balance for the whole layer. Then, the influence of temperature and solar irradiation on resulting short-circuit current, open-circuit voltage and power output is investigated through a comparison with existing data from literature. An insight into the thermal and electrical behaviors of the cell as a function of radiative and thermal boundary conditions is proposed to show the ability of the model to be used to find out and assess effective solutions to extract heat and to design cells for optimal photoelectric conversion performances.

2. Theoretical formulation

2.1. Problem description

The problem under consideration is described in Fig. 1. The generic structure of a photovoltaic (PV) module consists of a multilayer sandwich made of a PV cell, resin and glass layers, an antireflection coating and front and back contacts connected to an electrical load. The simplified configuration of a single P–N junction layer is considered for the sake of simplicity. Since the main objective is to evaluate PV module performances as a function of thermal and irradiation conditions, a comprehensive model of coupled conductive–radiative heat transfer including photoelectric phenomena which take place in the active part of a PV module is developed. Here a plane–parallel slab with homogeneous properties along the y- and z-axes

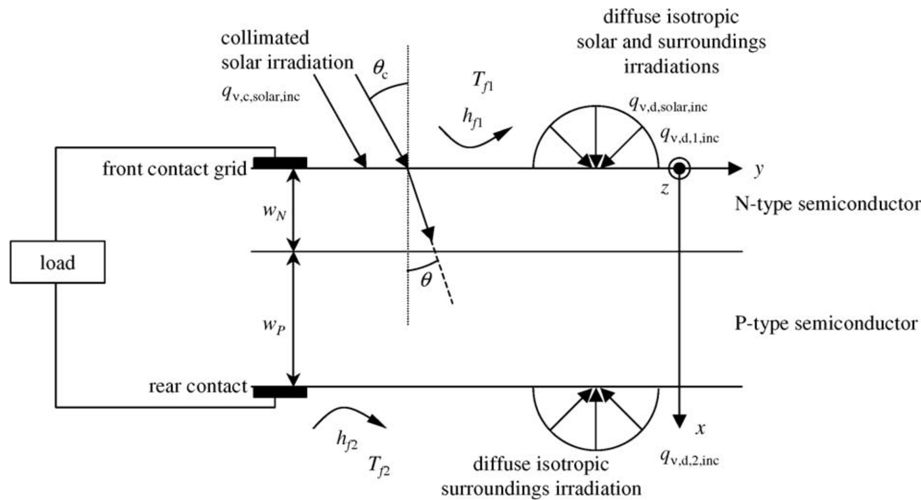

Fig. 1. Problem schematic description.

is studied, so that spatial variations are described in a one-dimensional Cartesian coordinate system. As a conventional PV cell, a standard P–N homo-junction is considered. It is made of a negatively doped upper zone (N-type region) and a positively doped lower zone (P-type region) of thickness w_N and w_P, respectively.

The cell upper face is subject to collimated and diffuse isotropic solar irradiation given by spectrally varying flux densities $q_{v,c,solar,inc}$ and $q_{v,d,solar,inc}$. The collimated beam is characterized by the incidence polar angle θ_c. Additional diffuse isotropic radiation fluxes ($q_{v,d,1,inc}$ and $q_{v,d,2,inc}$) are considered at both boundaries and refer to surroundings infrared radiation. The front and rear surfaces of the cell are assumed perfectly smooth and radiative boundary conditions are simply governed by Snell's law and Fresnel's equation. The junction exchanges heat by convection with the external fluid as a function of a constant convective heat transfer coefficient (respectively, h_{f1} at the upper face $x = 0$ and h_{f2} at the lower face $x = w_N + w_P$) and of the fluid free-stream or mean temperature (T_{f1} and T_{f2}).

To describe steady state coupled conductive—spectral radiative heat transfer within the cell, various thermophysical properties are required. The surrounding fluid is assumed non-absorbing and the real part of the complex refractive index ($n_{v,f}$) is constant and equal to unity. The semiconductor material is considered as an absorbing, emitting but non-scattering semitransparent medium. Spectral optical and radiative properties (n_v and κ_v) have to be determined as a function of wavelength and temperature. Several processes of absorption of light must be taken into consideration. Since frequency does not change with the refractive index whereas wavelength does, it is much better to express spectral variations as a function of frequency. The range investigated in the study is [2×10^{13}–1.13×10^{15} Hz], which matches the wavelength in vacuum range [0.27–15] μm. The upper wavelength limit is a consequence of a lack of knowledge for some radiative properties beyond it. The temperature field within the cell is governed by the steady state energy-balance equation which includes a temperature dependent thermal conductivity and local heat sources due to radiation absorption and thermal emission, charge carrier recombination mechanisms and excess power thermal release. The derivation of a solution to this problem requires the modeling of coupled spectral radiation, heat and carrier transport phenomena which take place within the cell. Next sections are devoted to the derivation of equations associated to the aforementioned processes and to the determination of required properties.

2.2. Semiconductor device physics

2.2.1. Elementary principles of P–N junctions and photovoltaic cells

A generic P–N junction is basically composed of three zones (Fig. 2(a)). The N-type semiconductor region ($x \in [0, w_N], w_N \sim 0.2$–$1$ μm) is negatively doped from the addition of pentavalent impurities (donor density N_d). At room temperature, dopants are contributing free electrons whose density is equal to the donor ion density ($n_e = N_d$). The P-type region ($x \in [w_N, w_N + w_P]$, $w_P \sim$ several hundreds of microns) is positively doped from the addition of trivalent impurities (acceptor density N_a) and at room temperature, it creates deficiencies of valence electrons—called holes—whose density is equal to the acceptor ion density ($n_h = N_a$). The N-type and P-type zones are in contact with each other and near the interface, some of the free electrons of the N-region diffuse across the junction towards the P-side whereas conversely holes diffuse from the P-side to the N-side. In the region near the interface, there are recombinations of electrons and holes. This gives rise to an excess of positive charges in the N-side (deplete of electrons) and of negative charges in the P-side (deplete of holes). This narrow intermediate region ($x \in [w_N - x_N, w_N + x_P]$) is called the depletion zone. An electric field (E_0) and a barrier potential (V_0) result from the opposite charge layers of ions and this creates forces which oppose

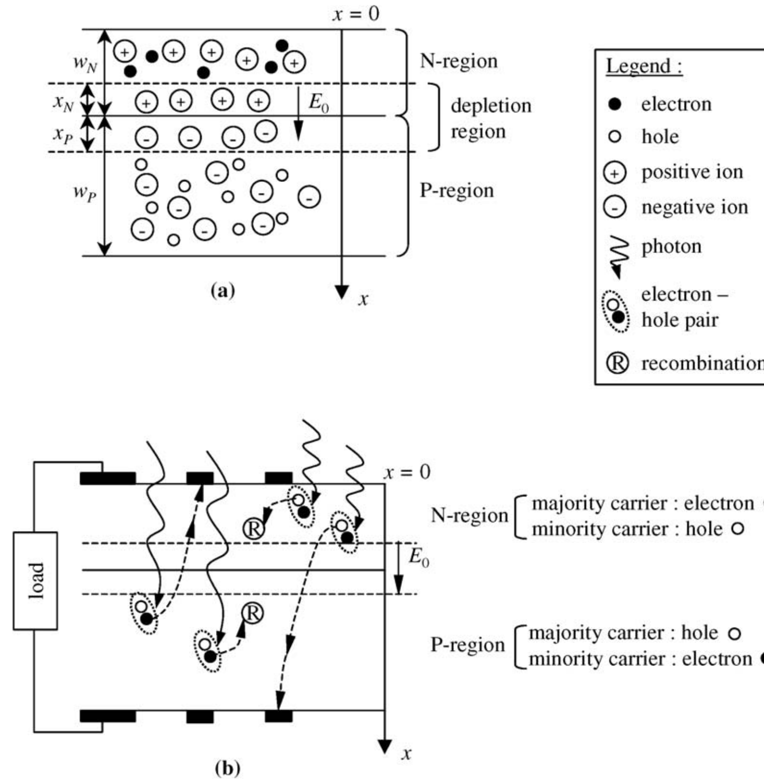

Fig. 2. Schematic description of: (a) a P–N junction at room temperature; (b) basic functioning principles of a photovoltaic cell.

to the electron and hole diffusion process. An equilibrium between resulting diffusion and drift-currents of carriers is then observed. In this situation, the predominant mobile charge (or majority) carriers are electrons in the N-side and holes in the P-side, and vice versa for minority carriers.

The functioning principle of a standard PV cell is described as follows (Fig. 2(b)). The preceding P–N junction is subject to radiative fluxes at the top of the N-type layer. Radiation is absorbed by semiconductor atoms along the path of radiation within the device. For photons with energy approximately larger than the energy gap (E_g) between valence and conduction electron energy bands, the absorption process creates mobile charge carriers in electron–hole pairs. A concentration gradient makes the minority carriers (holes for the N-side and electrons for the P-side) move. These minority carriers are pulled into the region where they are majority carriers by the electric field in the depletion region. Depending on where the minority carrier is created, it may either recombine before reaching the junction or cross the junction. If the junction is connected to an electrical load (with a forward bias of the P–N junction under an applied voltage V), a photocurrent is created and generates electrical power.

2.2.2. Minority carrier transport equations and photocurrent calculation

Minority carrier density is governed by the continuity equations, which in a one-dimensional planar system in steady state, are given as [8,9]

$$D_e \frac{d^2 \Delta n_e(x)}{dx^2} - \frac{\Delta n_e(x)}{\tau_e} + g_{op,\Delta\nu}(x) = 0 \quad \text{(P-region)}, \tag{1}$$

$$D_h \frac{d^2 \Delta n_h(x)}{dx^2} - \frac{\Delta n_h(x)}{\tau_h} + g_{op,\Delta\nu}(x) = 0 \quad \text{(N-region)}, \tag{2}$$

where for simplicity, the spectral dependence of parameters is specified only for the rate of minority carriers optically generated by local incident radiation for the frequency interval of width $\Delta\nu$ ($g_{op,\Delta\nu}(x)$). This rate comes from the solution of the radiative transfer problem and will be detailed in Section 2.3.2. $\Delta n_e(x)$ and $\Delta n_h(x)$ are the local excess of minority carriers created besides the equilibrium concentrations ($\Delta n_e = n_e - n_{e0}$ and $\Delta n_h = n_h - n_{h0}$). Equilibrium concentrations are given by $n_{e0} = n_i^2/N_a$ and $n_{h0} = n_i^2/N_d$, where n_i is the intrinsic carrier concentration (concentration of carriers for pure semiconductor material). D_e and D_h are the diffusion coefficients ($m^2\, s^{-1}$) of electrons and holes, respectively. The terms $\Delta n_e/\tau_e$ and $\Delta n_h/\tau_h$ are the recombination rate of minority carriers ($m^{-3}\, s^{-1}$), where τ_e and τ_h are the minority carrier lifetimes (s^{-1}) of electron and holes, respectively. Those continuity equations stand for electron density (n_e) in the P-region (Eq. (1)) and for holes density (n_h) in the N-region (Eq. (2)), which are quasi-neutral zones where the electric field vanishes so that minority carriers primarily flow by diffusion.

For the boundary condition at the depletion zone interface, all minority carriers are collected by the electric field so that the excess is zero

$$\Delta n_e|_{x=w_N+x_P} = 0 \quad \text{(P-region)}, \tag{3}$$

$$\Delta n_h|_{x=w_N-x_N} = 0 \quad \text{(N-region)}. \tag{4}$$

At the edges of the photovoltaic cell ($x = 0$ and $x = w_N + w_P$), recombination processes occur because of the presence of surface defects and of the metallic contacts. Associated recombination rates obey the following relations:

$$D_e \left.\frac{d\Delta n_e}{dx}\right|_{x=w_N+w_P} = S_e \Delta n_e|_{x=w_N+w_P} \quad \text{(P-region)}, \tag{5}$$

$$D_h \left.\frac{d\Delta n_h}{dx}\right|_{x=0} = S_h \Delta n_h|_{x=0} \quad \text{(N-region)}, \tag{6}$$

where S_e and S_h are surface recombination velocities (m s^{-1}) for electrons and holes, respectively.

Values for carrier diffusion coefficients, lifetimes, surface recombination velocities and intrinsic concentrations, including their possible dependence on temperature, are discussed in Section 2.4.2 for the specific case of a standard c-silicon photovoltaic cell.

The photocurrent densities generated in each zone are proportional to the gradient of minority carriers concentration at the depletion zone interfaces and are written as

$$J_e = qD_e \left.\frac{\partial n_e}{\partial x}\right|_{x=w_N+x_P} \quad \text{(P-region)}, \tag{7}$$

$$J_h = -qD_h \left.\frac{\partial n_h}{\partial x}\right|_{x=w_N-x_N} \quad \text{(N-region)}. \tag{8}$$

As for the depletion zone, the effect of recombination can be neglected so that all generated carriers cross the junction interface thanks to the electric field. Thus the associated current density is given by

$$J_{dz} = q \int_{w_N-x_N}^{w_N+x_P} g_{op,\Delta\nu}(x)\,dx. \tag{9}$$

The global photogenerated current density results from the summation of each zone contribution

$$J_{ph} = J_e + J_h + J_d. \tag{10}$$

Eventually, the total current density ($J_{ph,total}$) is obtained by summing up photocurrent densities over the frequency intervals $\Delta\nu$ for which carriers are optically generated.

2.2.3. Current–voltage characteristic

Depending on the load which is connected to the photovoltaic cell, the applied voltage (V) that appears across the junction has to be considered. This voltage disturbs the equilibrium of the junction and is responsible for a current flowing opposite to the photocurrent which is called diode current. When illuminated, the effective current density is then

$$J = J_{ph,total} - J_{diode}(V). \tag{11}$$

The diode current density is obtained from the solution of continuity equations (1) and (2) for dark conditions, i.e. the generation rate of minority carriers ($g_{op,\Delta\nu}$) is removed from the equations. Boundary conditions at the depletion zone interfaces are modified to take into account the applied voltage to give [8]

$$n_h|_{x=w_N-x_N} = \frac{n_i^2}{N_d} e^{\frac{qV}{kT}}, \tag{12}$$

$$n_e|_{x=w_N+x_P} = \frac{n_i^2}{N_a} e^{\frac{qV}{kT}}, \tag{13}$$

where k is the Boltzmann constant. Boundary conditions at the edges of the device are unaffected (Eqs. (5) and (6)).

The diode current density results from the sum of current densities due to the diffusion of holes and electrons at the edge of the depletion zone (Eqs. (7) and (8)). The curve of current variations as a function of the voltage (the so-called I–V characteristic), temperature and illumination conditions, is used to evaluate performances of the cell.

2.3. Spectral radiative and coupled heat transfer formulations

2.3.1. Heat transfer formulation

In a one-dimensional planar system, the differential equation of conduction at steady state with internal heat generation which governs the temperature profile is given by

$$\frac{d}{dx}\left\{k_c[T(x)]\frac{d}{dx}T(x)\right\} + Q(x) = 0, \tag{14}$$

where $k_c[T(x)]$ (W m^{-1} K^{-1}) is the local temperature dependent thermal conductivity and $Q(x)$ (W m^{-3}) is the local heat generation rate. For the specific—single cell—configuration under consideration, associated boundary conditions express that internal heat conduction is balanced by convection and non-radiative surface recombinations [10]

$$-k_c \left.\frac{dT}{dx}\right|_{x=0} = h_{f1}[T_{f1} - T(x=0)] + S_h E_g \sum_{\Delta\nu} \Delta n_h \Big|_{x=0} (\Delta\nu), \tag{15}$$

$$-k_c \left.\frac{dT}{dx}\right|_{x=w_N+w_P} = h_{f2}[T(x=w_N+w_P) - T_{f2}] + S_e E_g \sum_{\Delta\nu} \Delta n_e|_{x=w_N+w_P}(\Delta\nu), \tag{16}$$

where densities of optically generated minority carriers at the boundaries ($\Delta n_e|_{x=w_N+w_P}(\Delta\nu)$ and $\Delta\ n_h|_{x=0}(\Delta\nu)$) result from the solution of carrier transport equations.

From an analysis of the physical situation, the temperature gradient within the cell is expected to be small so that the heat transfer problem can be simplified by writing the thermal balance for the whole junction layer as

$$\left(\overbrace{\int_0^{w_N+w_P} Q(x)\,dx}^{q_{th,in}}\right) = \left(\overbrace{h_{f1}[T_{cell}-T_{f1}] + S_h E_g \sum\nolimits_{\Delta\nu} \Delta n_h|_{x=0}(\Delta\nu) + h_{f2}[T_{cell}-T_{f2}] + S_e E_g \sum\nolimits_{\Delta\nu} \Delta n_e|_{x=w_N+w_P}(\Delta\nu)}^{q_{th,out}}\right), \tag{17}$$

where a single temperature (T_{cell}) is considered and $q_{th,in}$ is the heat power generated within the whole layer. The cell temperature is easily extracted from the above equation.

In Eqs. (14) and (17), the local heat generation rate includes several sources or losses [10,11]

$$Q(x) = -S_r(x) + Q_T(x) + Q_{NRR}(x), \tag{18}$$

where $S_r(x)$ is the local total radiative source term, $Q_T(x)$ corresponds to the quasi-instantaneous thermalization of carriers to the band gap level (release of excess energy) and $Q_{NRR}(x)$ is due to the non-radiative recombinations of minority carriers.

The radiative contribution to the heat source due to absorption and thermal emission by free carriers or by the crystal lattice is given by

$$\begin{aligned} S_r(x) &= \int_0^{\infty} [\kappa_{\nu,fc}(x) + \kappa_{\nu,latt}(x)]\left\{4\pi n_\nu^2(x) I_{b,\nu}[T_{cell}] - G_\nu(x)\right\} d\nu \\ &= \sum_{\Delta\nu} [\kappa_{\Delta\nu,fc}(x) + \kappa_{\Delta\nu,latt}(x)]\left\{4\pi n_{\Delta\nu}^2(x) I_{b,\Delta\nu}[T_{cell}] - G_{\Delta\nu}(x)\right\}, \end{aligned} \tag{19}$$

where $G_{\Delta\nu}(x)$ is the local band incident radiation power obtained from the solution of the radiative transfer problem. The heat source from thermalization of photogenerated minority carriers to the band gap energy level is given as [10]

$$\begin{aligned} Q_T(x) &= \int_{h\nu > E_g} \frac{\kappa_{\nu,interband}(x) G_\nu(x)}{h\nu}(h\nu - E_g)\,d\nu \\ &= \sum_{\Delta\nu} \kappa_{\Delta\nu,interband}(x) \frac{G_{\Delta\nu}(x)}{\Delta\nu} \int_{\Delta\nu, h\nu > E_g} \left(1 - \frac{E_g}{h\nu}\right) d\nu, \end{aligned} \tag{20}$$

where the band gap energy is expressed in Joules.

For carrier recombination mechanisms, radiative recombination may be ignored for indirect band gap semiconductors such as silicon [12], whereas non-radiative recombination processes have to be considered and incorporated in the global heat source as [10]

$$Q_{NRR}(x) = \sum_{\Delta\nu} \frac{E_g}{\tau_e} \Delta n_e(x, \Delta\nu) \quad \text{(P-region)}, \tag{21}$$

$$Q_{NRR}(x) = \sum_{\Delta\nu} \frac{E_g}{\tau_h} \Delta n_h(x, \Delta\nu) \quad \text{(N-region)}, \tag{22}$$

where τ_e and τ_h are the minority carrier lifetimes (s^{-1}) of electrons and holes, respectively, $\Delta n_e(x, \Delta\nu)$ and $\Delta n_h(x, \Delta\nu)$ are the densities of local excess of minority carriers optically generated by local incident radiation for the frequency interval of width $\Delta\nu (g_{op,\Delta\nu}(x))$ and are obtained from the solution of carrier transport equations (see Section 2.2.2).

2.3.2. Radiative transfer equation

For a one-dimensional planar problem with an absorbing, emitting and non-scattering isothermal medium, under the assumption of azimuthal symmetry, the gray-band formulation of the radiative transfer equation (RTE) for unpolarized radiation is given by

$$\mu \frac{dI_{\Delta\nu}(x,\mu)}{dx} = \kappa_{\Delta\nu}(x)\left\{n_{\Delta\nu}^2 I_{b,\Delta\nu}[T_{cell}] - I_{\Delta\nu}(x,\mu)\right\}, \tag{23}$$

where $I_{\Delta\nu}$ is the band intensity ($I_{\Delta\nu} = \int_{\Delta\nu} I_\nu\, d\nu$), $I_{b,\Delta\nu}[T_{cell}]$ is the Planck function in vacuum integrated over the frequency interval $\Delta\nu$. $\kappa_{\Delta\nu}$ and $n_{\Delta\nu}$ are, respectively, the absorption coefficient and refractive index averaged over the frequency interval $\Delta\nu$ and μ is the cosine of the polar angle of the direction ($\mu = \cos\theta$, Fig. 1). The absorption coefficient is obtained from the summation of absorption coefficients associated to several optical processes and is written as (monochromatic case)

$$\kappa_\nu = \kappa_{\nu,interband} + \kappa_{\nu,fc} + \kappa_{\nu,latt}, \tag{24}$$

where $\kappa_{\nu,interband}$ refers to the interband absorption—i.e. electronic transitions from the valence to the conduction band—, $\kappa_{\nu,fc}$ and $\kappa_{\nu,latt}$ stand for optical absorption processes operated by free carriers and the crystal lattice, respectively. Expressions and/or values for radiative and optical properties will be given in Section 2.4.1 for the case of c-silicon.

Radiative boundary conditions involving refraction of external collimated and diffuse irradiation at the top of the layer are simply governed by Snell's law and Fresnel's equation, which are considered to depend only on the real part of the complex refractive index and on the angle of incidence. Additional details are given in a previous paper [13].

From the solution of the radiative transfer equation, the local band incident radiation power is obtained from

$$G_{\Delta\nu}(x) = 2\pi \int_{-1}^{1} I_{\Delta\nu}(x,\mu)\,d\mu, \tag{25}$$

and the local rate of minority carriers $g_{op,\Delta\nu}(x)$ optically generated on the frequency interval $\Delta\nu$ which is requested for the carrier transport equations (1) and (2) is written as

$$\begin{aligned} g_{op,\Delta\nu}(x) &= \int_{\Delta\nu} \frac{\kappa_{\nu,interband}(x) G_\nu(x)}{h\nu} d\nu \\ &= \kappa_{\Delta\nu,interband}(x) \frac{G_{\Delta\nu}(x)}{\Delta\nu} \int_{\Delta\nu} \frac{1}{h\nu} d\nu \end{aligned} \tag{26}$$

2.4. Optical, radiative and thermophysical properties of c-silicon

From this section, the study is restricted to the case of crystalline silicon homo-junctions. Optical, radiative and thermophysical properties requested in the physical modeling described in previous sections are then specifically given for c-silicon. In particular, the energy band gap E_g used in Eqs. (15)–(17) and (20)–(22) is the fundamental indirect energy gap of silicon (E_{g1} (300 K) = 1.12 eV).

2.4.1. Optical and radiative properties

Radiation absorption in the silicon junction occurs through several quantum processes. The so-called interband absorption mechanism corresponds to electronic transitions from the valence to the conduction band. In the case of silicon, which is an indirect band gap semiconductor, absorption of photons through the interband mechanism may involve phonon emission or absorption. Accordingly, an expression for the absorption coefficient has been derived by Rajkanan et al. [14]

$$\kappa_{\nu,\text{interband}}(T) = \sum_{i=1,2}\sum_{j=1,2} C_i A_j \left[\frac{\{h\nu - E_{gj}(T) + E_{pi}\}^2}{\exp(E_{pi}/kT) - 1} + \frac{\{h\nu - E_{gj}(T) - E_{pi}\}^2}{1 - \exp(-E_{pi}/kT)}\right] + A_d[h\nu - E_{gd}(T)]^{1/2}, \tag{27}$$

where the last term corresponds to the direct transition, the first term is comprised of summations on indirect transitions ($j = 1,2$; energy band gaps E_{gj}) and on the type of phonon which assists the transition (transverse optical or acoustic, $i = 1,2$; energy E_{pi}). Temperature dependence of energy band gaps can be written by using the Varshni equation [15]

$$E_g(T) = E_g(0) - \frac{\beta T^2}{T + \gamma}, \tag{28}$$

where parameters β and γ are adjusted to fit with experimental data. Various sets of parameters are reported in the review by Weber (in [15]). In this paper, the ones obtained by Alex et al. [16] from recent experiments are used, instead of the set given by Rajkanan et al. [14] for the calculation of the interband absorption coefficient formula (see Table 1).

With parameters for Eqs. (27) and (28) reported in Table 1, values of the absorption coefficient obtained have been checked to correlate closely with experimental data for intrinsic silicon at 300 K given in the compilation databases from Refs. [15,17] (Fig. 3(a)). The temperature dependence

Table 1
Parameters for the calculation of the interband absorption coefficient and the temperature dependent correlation for the energy band gaps of silicon

Ref.	Parameter	Value	Parameter	Value
Ref. [14]	E_{p1} (eV)	1.83×10^{-2}	A_1 (cm^{-1} eV^{-2})	323.1
	E_{p2} (eV)	5.77×10^{-2}	A_2 (cm^{-1} eV^{-2})	7237
	$E_{gd}(0)$ (eV)	3.2	A_d (cm^{-1} eV^{-2})	1.05×10^{-6}
	$E_{g2}(0)$ (eV)	2.5	C_1	5.5
	$E_{g1}(0)$ (eV)	1.1557	C_2	4
	β (eV/K)	7.021×10^{-4}	γ (K)	1108
Ref. [16]	$E_{g1}(0)$ (eV)	1.1692		
	β (eV/K)	4.9×10^{-4}	γ (K)	655

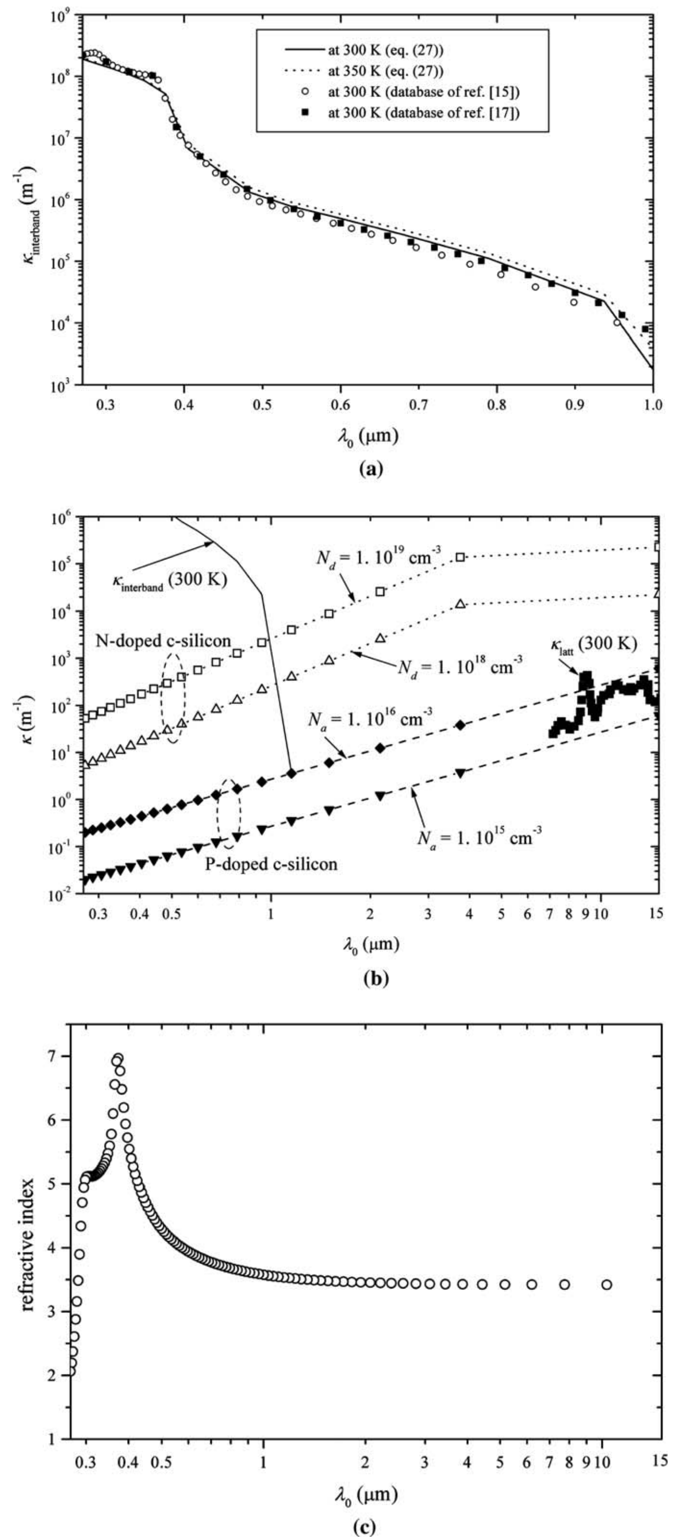

Fig. 3. Optical properties of c-silicon: (a) calculation of the interband absorption coefficient and comparison with datareviews from refs. [15,17] for intrinsic c-silicon at 300 K; (b) free-carrier absorption coefficient as a function of the doping level and infrared lattice absorption coefficient [19]; (c) refractive index at 300 K [15].

of this absorption coefficient may be illustrated by its percentage increase for a temperature step from 300 K to 350 K, which is found to be comprised between 4.7% and 41.4% in the [0.27–1] μm wavelength in vacuum range.

The free-carrier absorption coefficient $\kappa_{\nu,\mathrm{fc}}$ (m^{-1}) is taken from the empirical model reported in Ref. [18]

$$\kappa_{\nu,\mathrm{fc}} = 260\left(\frac{c_0}{\nu}\right)^3 n_\mathrm{e}, \quad \lambda_0 \leqslant 5\ \mu\mathrm{m}$$
$$\kappa_{\nu,\mathrm{fc}} = 1.10^4\left(\frac{c_0}{\nu}\right)^2 n_\mathrm{e}, \quad \lambda_0 > 5\ \mu\mathrm{m} \tag{29}$$

$$\kappa_{\nu,\mathrm{fc}} = 2.710^{-4}\left(\frac{c_0}{\nu}\right)^2 n_\mathrm{h} \quad \text{(P-region)}, \tag{30}$$

where c_0 is the light speed in vacuum ($\mathrm{m\,s^{-1}}$), ν is the frequency (Hz), λ_0 is the corresponding wavelength in vacuum, n_e and n_h (cm^{-3}) are the majority carrier concentrations, respectively, equal to N_d and N_a under the assumption that around room temperature all dopants are ionized. Fig. 3(b) depicts the variations of this coefficient as a function of doping level. It is observed that the free-carrier absorption coefficient is negligible for wavelengths below 1 μm in comparison with the interband absorption coefficient.

Radiation may also be absorbed by the crystal lattice. The absorption coefficient relative to this phenomenon in the infrared range $\lambda_0 \in [7.14\text{–}15]$ μm is taken from Ref. [19] and is depicted in Fig. 3(b). It is observed that it is often small when compared with the free-carriers absorption coefficient, except for low doping concentrations.

As for spectral values for the real part of crystalline silicon complex refractive index, they are taken among several existing databases from the compilation given in Ref. [15] (Fig. 3(c)).

2.4.2. Thermophysical properties

Thermal conductivity of bulk c-silicon varies with temperature. The correlation derived from experiments by Glassbrenner and Slack [20], valid in the temperature range [250–600] K, is given as

$$k_\mathrm{c}(T) = \frac{100}{0.03 + 1.5610^{-3}T + 1.6510^{-6}T^2}, \tag{31}$$

where T and k_c are expressed in K and $\mathrm{W\,m^{-1}\,K^{-1}}$, respectively. The influence of doping is reported to be substantial for high injection levels ($\sim 10^{20}\ \mathrm{cm}^{-3}$) and larger for decreasing temperatures below 300 K [21]. Thermal conductivity of bulk c-silicon used in this paper is found to vary between 125 and 175 $\mathrm{W\,m^{-1}\,K^{-1}}$ for temperatures comprised within the range [270–360 K].

As for carrier transport modeling in illuminated (Eqs. (1)–(6)) and dark conditions (Eqs. (1), (2), (5), (6), (12) and (13)), diffusion coefficients, recombination rates, surface recombination velocities and intrinsic concentration of minority carriers have to be determined as input data. Those physical parameters generally depend on temperature, type of silicon (method of crystal growth for c-silicon) and doping concentrations.

For c-silicon, a literature analysis exhibits (see the review in [15]) some discrepancies between existing experimental values and also between formulas. Consequently, since a discussion on these aspects are out of the scope of this work, our selection is subjected to improvements depending on the design and fabrication of precise devices under consideration. In this work, diffusion coefficients, mobilities and recombination rates are calculated by applying selected formulations [15,22] reported in Table 2. Recombination velocity is related to the boundary surface state (passivation techniques, metallic collector surface covering). It is quite difficult to choose an accurate value for this parameter except if experimental values are available for the cell under consideration.

The intrinsic carrier concentration depends on temperature and is given by [8,15]

$$n_\mathrm{i}^2 = N_\mathrm{C}(T)N_\mathrm{V}(T)\mathrm{e}^{-E_{\mathrm{g1}}(T)/kT} = N_\mathrm{C}(300\ \mathrm{K})\left(\frac{T}{300}\right)^{3/2} N_\mathrm{V}(300\ \mathrm{K})\left(\frac{T}{300}\right)^{3/2}\mathrm{e}^{-E_{\mathrm{g1}}(T)/kT}, \tag{32}$$

Table 2
Formulas and associated constants used for the calculation of lifetime [15], diffusion coefficient and mobility [22] of minority carriers for c-silicon

	Electrons	Holes
Lifetime [15]	$\tau_\mathrm{e} = \frac{1}{3.45\times10^{-12}N_\mathrm{a} + 9.5\times10^{-32}N_\mathrm{a}^2}$ (s), $N_\mathrm{a} \geqslant 10^{17}\ \mathrm{cm}^{-3}$, N_a in cm^{-3}, $\tau_\mathrm{e} = 2.89\times10^{-6}$ s, $N_\mathrm{a} < 10^{17}\ \mathrm{cm}^{-3}$	$\tau_\mathrm{h} = \frac{1}{7.8\times10^{-13}N_\mathrm{d} + 1.8\times10^{-31}N_\mathrm{d}^2}$ (s), $N_\mathrm{d} \geqslant 10^{17}\ \mathrm{cm}^{-3}$, N_d in cm^{-3}, $\tau_\mathrm{h} = 12.5\times10^{-6}$ s, $N_\mathrm{d} < 10^{17}\ \mathrm{cm}^{-3}$
Diffusion coefficient (Einstein relation)	$D_\mathrm{e} = \mu_\mathrm{e}\frac{kT}{q}$ ($\mathrm{m^2\,s^{-1}}$), all parameters in SI units	$D_\mathrm{h} = \mu_\mathrm{h}\frac{kT}{q}$ ($\mathrm{m^2\,s^{-1}}$), all parameters in SI units
Mobility [22]	$\mu_\mathrm{e} = \mu_{\mathrm{e,min}} + \frac{\left(\mu_{\mathrm{e},0}\left(\frac{T}{300}\right)^{\nu_\mathrm{e}} - \mu_{\mathrm{e,min}}\right)}{1 + \left(\frac{T}{300}\right)^{\xi_\mathrm{e}}\left(\frac{N_\mathrm{a}}{n_{\mathrm{e,ref}}}\right)^{\alpha_\mathrm{e}}}$ ($\mathrm{cm^2\,V^{-1}\,s^{-1}}$) with: $\mu_{\mathrm{e,min}} = 55.24\ \mathrm{cm^2\,V^{-1}\,s^{-1}}$, $\mu_{\mathrm{e},0} = \mu_\mathrm{e}$ (300 K) $= 1350\ \mathrm{cm^2\,V^{-1}\,s^{-1}}$, $\nu_\mathrm{e} = -2.3$, $\xi_\mathrm{e} = -3.8$, $\alpha_\mathrm{e} = 0.73$, $n_{\mathrm{e,ref}} = 1.072\times10^{17}\ \mathrm{cm}^{-3}$, N_a in cm^{-3}	$\mu_\mathrm{h} = \mu_{\mathrm{h,min}} + \frac{\left(\mu_{\mathrm{h},0}\left(\frac{T}{300}\right)^{\nu_\mathrm{h}} - \mu_{\mathrm{h,min}}\right)}{1 + \left(\frac{T}{300}\right)^{\xi_\mathrm{h}}\left(\frac{N_\mathrm{d}}{n_{\mathrm{h,ref}}}\right)^{\alpha_\mathrm{h}}}$ ($\mathrm{cm^2\,V^{-1}\,s^{-1}}$) with: $\mu_{\mathrm{h,min}} = 49.7\ \mathrm{cm^2\,V^{-1}\,s^{-1}}$, $\mu_{\mathrm{h},0} = \mu_\mathrm{h}$ (300 K) $= 480.\ \mathrm{cm^2\,V^{-1}\,s^{-1}}$, $\nu_\mathrm{h} = -2.2$, $\xi_\mathrm{h} = -3.7$, $\alpha_\mathrm{h} = 0.70$, $n_{\mathrm{h,ref}} = 1.606\times10^{17}\ \mathrm{cm}^{-3}$, N_d in cm^{-3}

where $E_{g1}(T)$ is the fundamental indirect band gap of silicon whose variations with temperature are given by Eq. (27). $N_C(T)$ and $N_V(T)$ are the effective densities of states in the conduction and valence bands, respectively, equal to $2.8 \times 10^{19}\ \mathrm{cm}^{-3}$ and $1.04 \times 10^{19}\ \mathrm{cm}^{-3}$ at 300 K for silicon.

3. Solution methods

3.1. Minority carrier density from the solution of continuity equations

Minority carrier density is calculated by solving the continuity equations (Section 2.2.2) for the two zones of the junction. Those equations belong to general boundary value problems consisting of an ordinary differential equation with side conditions specified at more than one point. The shooting method [23] is well suited to get a numerical solution. It has been applied and validated against analytical solutions for a simplified configuration [8]. In this situation, the Beer-law (exponential decrease of the incident radiation power in the layer) is considered so that the minority carrier generation rate has the simple form

$$g_{\mathrm{op},\Delta\nu}(x) = C_1 \mathrm{e}^{-C_2 x}, \tag{33}$$

where C_1 and C_2 are constants. Numerical results obtained by applying the shooting method have been checked to match very well with analytical solutions for a wide range of parameters.

3.2. Radiative transfer and energy balance equations solution methods

The conduction–radiation heat transfer problem for a multilayer slab (see for example [24]) with Fresnel interfaces subject to diffuse and obliquely collimated irradiation is solved by means of a method that we described in a previous paper [13]. Thus only main features will be given hereafter. The incident collimated radiation flux is treated separately from the diffuse irradiation [25,26]. The local spectral incident radiation power originating from the collimated component is derived through the development of analytical formulas by using a Ray Tracing (RT) procedure which accounts for the exponential attenuation of radiation along the path of rays and for the multireflections between boundaries of the junction layer. As for the problem of the radiation diffuse component, a numerical solution of the radiative transfer equation (Eq. (23)) is provided by means of a composite discrete ordinates method (CDOM) [27]. It basically corresponds to a standard discrete ordinates method [28] with a specific feature which consists of the cutting of the directional integration into subintervals in accordance with the critical angles associated to the interfaces [13,29]. Then the discrete ordinate set varies as a function of the spectrally varying optical properties of the junction layer and are generated for each frequency interval ($\Delta\nu$). The radiative transfer solution methods have been validated previously against Monte Carlo predictions [13]. It is worth noticing that the local rate of minority carriers $g_{\mathrm{op},\Delta\nu}(x)$ optically generated on the frequency interval $\Delta\nu$ (Eq. (26)) is obtained from the local spectral incident radiation power resulting from both collimated and diffuse radiation components.

The local formulation of the heat transfer problem (Eqs. (14)–(16)) is solved by using a standard finite difference procedure which has also been validated [13] against reference results in the case of coupled radiation–conduction heat transfer within a gray plane–parallel medium confined between opaque black boundaries [29]. The simplified approach to solve the heat transfer problem by writing the thermal balance for the whole junction layer has been confronted with results obtained with the method which considers the local formulation for a set a representative situations. It has been found that the resulting temperature profile which effectively takes place into the cell exhibits very weak temperature gradients (<0.01 K). Moreover, the cell temperature derived from local and simplified formulations are quite the same (0.5% maximum relative discrepancy). As a consequence, in the following, the simplified approach will be used so that we will refer to a unique cell temperature (T_{cell}).

Carrier transport, radiative transfer and energy balance equations are coupled to each other which implies that a specific iterative procedure has to be implemented.

3.3. Solution of the coupled spectral radiative—thermal—carrier transport problems

To solve the whole problem involving several interdependent physical phenomena, the iterative procedure starts by solving the heat transfer problem. The solution of the cell energy balance equation provides the cell temperature. It is then possible to solve the radiative transfer problem for both collimated and diffuse components and for each spectral band. As a result, local total radiative and thermalization heat sources are calculated, as well as local rates of optically generated minority carriers $g_{\mathrm{op},\Delta\nu}(x)$. This leads to the next step which consists in solving the carriers transport equations to get the density profiles. Boundary values are stored and local heat sources which are associated to the non-radiative recombinations are evaluated to complete the estimation of the total heat source. Both have to be inserted in the energy balance equation at the next iteration. The determination of the photocurrent ends the iteration before convergence criteria on successive temperature and heat power generated within the cell are checked to decide whether a new iteration has to be executed or not.

Once convergence is achieved, carrier diffusion coefficients are updated using the final cell temperature to calculate the diode current through the solution of continuity equations in dark conditions with associated boundary conditions and for applied voltages from zero to the

open-circuit value (V_{oc}). Final results are the cell temperature, the current–voltage characteristic and numerous intermediate quantities such as radiative, thermalization and non-radiative recombination local heat sources which may be useful for advance analysis.

A special attention has to be paid to the spatial discretizations employed to get a numerical solution of the equations associated to three different physical phenomena. First, carrier transport equations are solved separately for the N and P regions. For standard silicon cells, the N-region and P-region thicknesses are quite different, i.e. less than 1 micron and equal to several hundreds of microns, respectively. Moreover, diffusion lengths are not the same for holes (~micron) in the N-region and for electrons (~mm) in the P-region. Discrete layer numbers used for the numerical solution of carrier continuity equations are chosen accordingly. In order to solve the radiative transfer problem, the critical parameter is the optical thickness of discrete layers ($\Delta\tau_{\Delta\nu} = \kappa_{\Delta\nu}\Delta x$) which should be less than unity. This optical thickness is related to the absorption coefficient magnitude for each frequency band, which reaches up to $2 \times 10^8\ \mathrm{m}^{-1}$ at the shortest wavelengths. Finally, since local rates of optically generated carriers ($g_{op,\Delta\nu}(x)$) required for the carriers transport problem are resulting from the radiative transfer problem solution, a correspondence between meshings used for radiative transfer and carrier transport problems has to be carried out. The simplest approach is applied: it consists in choosing a unique set of discrete layers numbers (M_N and M_P) for N and P zones which respect the aforementioned conditions for carrier and radiation transport equations. Since continuity equations have to be solved at the two boundaries of each zone, carrier densities are evaluated at the limits of discrete layers whereas radiative quantities are calculated at the center.

4. Application, results and analysis

4.1. Selected parameters and cases

In addition to c-silicon properties evaluated in Section 2.4, many other parameters have to be selected for the application section: P and N layer widths are $w_P = 400\ \mu\mathrm{m}$ and $w_N = 0.4\ \mu\mathrm{m}$, respectively. Widths of the N-side and P-side (Fig. 2(a)) of the depletion zone (x_N and x_P) depend on the concentration of dopants and on the voltage V. In the situation under consideration ($N_a = 1.5 \times 10^{15}\ \mathrm{cm}^{-3}$ and $N_d = 5 \times 10^{19}\ \mathrm{cm}^{-3}$), they have been found to be negligible in comparison with the P and the N region ones. Surface recombination velocities are chosen to be $S_e = 10\ \mathrm{m\ s}^{-1}$ and $S_h = 1\ \mathrm{m\ s}^{-1}$ for P and N zones, respectively.

Standard diffuse and collimated solar spectra have been defined about more than twenty years ago. However, for better photovoltaic cell performance evaluation, up to date spectral atmospheric transmission models are now available [30]. In this work, among several more or less sophisticated approaches, we choose to use the simple SPCTRL2 code from Bird [31] which is appropriate for the spectral discretization applied in our own modeling. Solar direct and diffuse components are obtained for any incidence and for specific location on earth, time and atmosphere properties. 16 frequency intervals are selected to be able to represent variations of all spectral quantities (solar irradiation, refractive index, absorption coefficients). Band integrated values of solar fluxes are calculated by applying a trapeze integration method.

Table 3
Application cases: thermal and radiative boundary conditions

Case	1.a	1.b	1.c	1.d	2.a	2.b	2.c
$q_{c,solar,inc}$ ($\mathrm{W\ m}^{-2}$)			707.9			822	
$q_{d,solar,inc}$($\mathrm{W\ m}^{-2}$)			229			257.2	
$T_{f1} = T_{surr,1}$ (°C)			5			25	
$T_{f2} = T_{surr,2}$ (°C)			5			25	30
h_{f1} ($\mathrm{W\ m}^{-2}\ \mathrm{K}^{-1}$)				5			
h_{f2} ($\mathrm{W\ m}^{-2}\ \mathrm{K}^{-1}$)		5	$\to\infty$ (5000)	0		5	10
$q_{d,1,inc}$ ($\mathrm{W\ m}^{-2}$)	0		173.4		0	250.7	
$q_{d,2,inc}$ ($\mathrm{W\ m}^{-2}$)	0		173.4		0	250.7	273.4

As for additional diffuse isotropic irradiation which may come from the surroundings, for the sake of simplicity, they are chosen to be defined by a blackbody emission at given surroundings temperatures ($T_{surr,1}$ and $T_{surr,2}$) which are assumed to be equal to the fluid temperatures. More realistic boundary conditions will be considered for future work.

Once some of the numerous parameters of the problem are fixed, several cases are investigated in this paper. The main objective is to analyze the thermal and electrical behaviors of the PV cell as a function of various radiative and thermal boundary conditions (see Table 3). A winter (cases 1.a–1.d) and a summer (cases 2.a–2.c) solar irradiation situations for western Europe are treated and a normal incidence is considered. For the cell side subjected to solar irradiation, external fluid and surroundings temperatures are chosen accordingly (resp. 5 °C and 25 °C) and heat exchange between the fluid and the cell is governed by natural convection with $h_{f1} = 5\ \mathrm{W\ m}^{-2}\ \mathrm{K}^{-1}$. Cases are unlike each other in the definition of possible additional surroundings irradiation and of the type of thermal boundary condition at side 2 of the cell.

4.2. Results and analysis

4.2.1. Consistency of the numerical model for radiation heat transfer

Given the complexity of the radiation heat transfer problem, it is worth checking the degree of accuracy of the model. Such a test is made possible by analyzing the radiation balance resulting from the convergence of the numerical model. Considering the unit area of the junction layer as the system, the radiation power balance equation is written as following (Fig. 4):

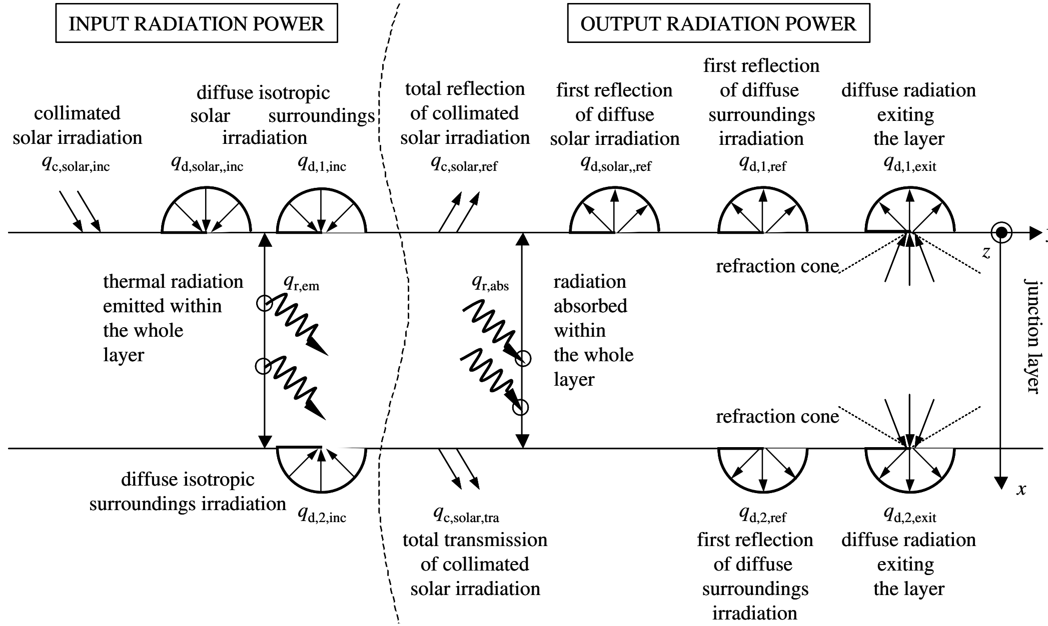

Fig. 4. Schematic representation of fluxes which are involved in the radiation power balance of the junction layer system.

$$\left(\overbrace{q_{c,solar,inc}+q_{d,solar,inc}+q_{d,1,inc}+q_{d,2,inc}+q_{r,em}}^{q_{r,in}}\right) - \left(\underbrace{q_{c,solar,ref}+q_{c,solar,tra}+q_{d,solar,ref}+q_{d,1,ref}+q_{d,2,ref}+q_{d,1,exit}+q_{d,2,exit}+q_{r,abs}}_{q_{r,out}}\right) = 0 \tag{34}$$

where all terms correspond to total radiation power per unit junction layer surface (W m^{-2}) which are calculated by a summation over all frequency bands. The total collimated ($q_{c,solar,inc}$) and diffuse ($q_{d,solar,inc}$) solar irradiation as well as surroundings diffuse irradiation on both sides ($q_{d,1,inc}$ and $q_{d,2,inc}$) are input data. $q_{r,em}$ corresponds to the total thermal radiation power emitted within the whole layer and is obtained from the final solution of the radiative transfer equation and from the cell temperature (this is the summation over the layer thickness of the emission term in the radiation source given by Eq. (19)). As for the system radiation losses, they result from: the total reflection and transmission of the collimated solar irradiation ($q_{c,solar,ref}$ and $q_{c,solar,tra}$) including multiple reflections within the layer which is obtained from the solution of the radiative transfer problem for the collimated part (Section 3.2); the first reflection of all diffuse irradiations ($q_{d,solar,ref}$, $q_{d,1,ref}$ and $q_{d,2,ref}$), calculated through the application of Snell's and Fresnel's reflection laws with a classical quadrature summation rule to get fluxes; the diffuse radiation exiting the layer at the top and bottom faces ($q_{d,1,exit}$ and $q_{d,2,exit}$), which result from the solution of the radiative transfer problem for the diffuse component (CDOM) and from the transmission through interfaces of intensities whose directions are included in the refraction cone; the radiation power absorbed through all processes within the whole layer (absorption term of Eq. (19) with the addition of the interband absorption coefficient to take into account all processes). All those radiation fluxes have been computed and it has been found that the relative difference between input ($q_{r,in}$) and output ($q_{r,out}$) radiation fluxes does not exceed 2.5% for all cases treated in this paper.

4.2.2. Consistency of the global model: influence of temperature and solar irradiation

Even if all models have been validated separately for academic reference cases (Sections 3.1 and 3.2), the convenient way to check the validity of both physical and numerical models is to make comparisons with experimental data for given situations. Unfortunately, although such kind of data might be found from literature, a complete and accurate comparison is not possible because of a lack of information concerning the experimental conditions and the values of the numerous parameters required

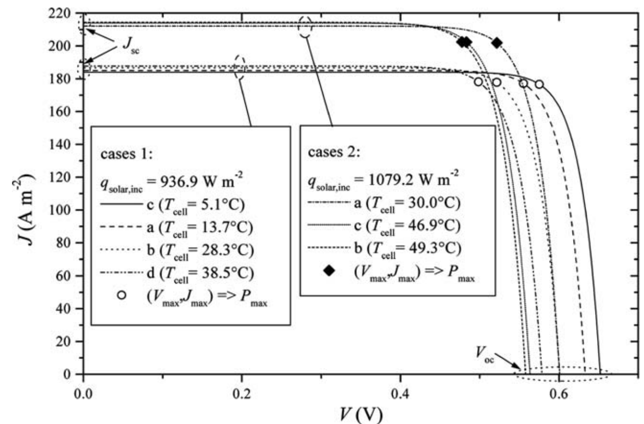

Fig. 5. *I–V* characteristic and cell temperature for application cases.

Table 4
Resulting I–V characteristic parameters as a function of cell temperature

$q_{\mathrm{solar,inc}}$ (W m^{-2})	936.9				1079.2		
T_{cell} (°C)	5.1	13.7	28.4	38.5	30.0	46.9	49.3
case	1.c	1.a	1.b	1.d	2.a	2.c	2.b
$P_{\max}$ (W m^{-2})	101.6	98.3	92.8	88.8	105.3	97.8	96.7
η_{el} (%)	10.84	10.49	9.91	9.48	9.76	9.06	8.96
$\frac{1}{P_{\max}}\frac{\mathrm{d}P_{\max}}{\mathrm{d}T_{\mathrm{cell}}}$ (K^{-1})	−0.0040				−0.0044		
J_{sc} (A m^{-2})	184.1	185.1	186.6	187.7	212.2	214.1	214.4
$\frac{1}{J_{\mathrm{sc}}}\frac{\mathrm{d}J_{\mathrm{sc}}}{\mathrm{d}T_{\mathrm{cell}}}$ (K^{-1})	0.00059				0.00056		
V_{oc} (V)	0.652	0.63	0.601	0.578	0.601	0.563	0.558
$\frac{1}{V_{\mathrm{oc}}}\frac{\mathrm{d}V_{\mathrm{oc}}}{\mathrm{d}T_{\mathrm{cell}}}$ (K^{-1})	−0.0036				−0.0038		

in the actual detailed model. Thus we are only able to validate the order of magnitude of our results by comparing the temperature and electrical efficiency obtained from the model (for the chosen standard values of doping and geometric parameters) with general trends known from literature.

For all cases treated in this paper, calculated current density (J)–voltage (V) characteristics are reported in Fig. 5. The particular operating point ($J_{\max}$, $V_{\max}$) which maximizes electric output power ($P_{\max}$) is pointed out. Curves are displayed to separate the two situations of solar irradiation (case 1: $q_{\mathrm{solar,inc}} = 936.9$ W m^{-2} and case 2: $q_{\mathrm{solar,inc}} = 1079.2$ W m^{-2}) and for each of them, the legend is ordered by increasing resulting cell temperatures, which in addition to solar irradiance depend on thermal and surroundings irradiation boundary conditions (see also Table 4). Those results are in agreement with typical ones reported in literature (see Ref. [8] and the review in [1]) in the sense that:

- the maximum electric output power ($P_{\max}$) naturally increases with solar irradiation,
- for a given solar irradiation, the short-circuit current density (J_{sc}) slightly increases with temperature with a mean increase rate ($1/J_{\mathrm{sc}}\,\mathrm{d}J_{\mathrm{sc}}/\mathrm{d}T_{\mathrm{cell}}$) equal to 0.059%/K and 0.056%/K for cases 1 and 2, respectively (typical values of 0.033%/K and 0.06%/K reported in [1]). This partially comes from a drop of the energy band gap (Eq. (28)) which leads to an increase of the interband absorption coefficient (Fig. 3(a)), corresponding to more photogenerated carriers viz. a gain in photocurrent,
- for a given solar irradiation, the open-circuit voltage (V_{oc}) noticeably diminishes with a mean decrease rate ($1/V_{\mathrm{oc}}\,\mathrm{d}V_{\mathrm{oc}}/\mathrm{d}T_{\mathrm{cell}}$) equal to −0.36%/K for case 1 and −0.38% for case 2 (typical value of −0.4%/K reported in [1]),
- as a result, for a given solar irradiation, $P_{\max}$ (consequently the photoelectric conversion efficiency η_{el}) decreases with rising temperature, with a mean decrease rate ($1/P_{\max}\,\mathrm{d}P_{\max}/\mathrm{d}T_{\mathrm{cell}}$) equal to −0.4%/K and −0.44%/K for cases 1 and 2, respectively (typical values comprised between −0.4%/K and −0.5%/K in [8]; other values of −0.4%/K and −0.65%/K reported in [1]).

It should be emphasized that calculated photoelectric efficiencies (from 9% to 11%) are slightly small when compared with the usual order of magnitude for commercial PV silicon cells (11–14%) for the reason that no antireflection coating is considered in the actual model. The central result is that main effects of increasing temperature are consistently and accurately evaluated by the model which means that it may be used for a detailed analysis of thermal and electrical behaviors resulting from thermal and radiative boundary conditions selected for application cases.

4.2.3. Insight into thermal and electrical behaviors as a function of thermal and radiative boundary conditions

The cell equilibrium temperature achieved for each case may be explained from extracting appropriate links between boundary conditions and some physical variables provided by the model. This may be illustrated from cases 2 by analyzing the spatial variations of the local total heat source $Q(x)$ (Eq. (18)) in Fig. 6. Main differences are

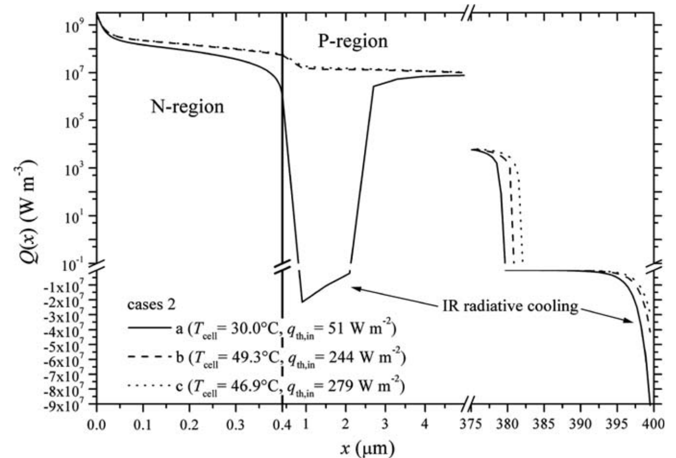

Fig. 6. Spatial variations of the total internal heat power.

observed between case 2.a and cases 2.b–c in the top part of the layer ($x \in [0, 5]$ μm): the total heat source is much lower for case 2.a than for the two other ones. Since no surroundings irradiation is considered for case 2.a, emission of thermal radiation is much more important than absorption near boundaries. Thus for spectral bands 1, 2, 3 and 4 ($\lambda_0 \in [2.5, 15]$ μm) a negative local radiative source term ($-S_{r,\Delta\nu}(x)$) is the cause of a significant lowering of the total heat source. As a result, the heat power generated within the whole layer ($q_{th,in}$, Eq. (17)) is much lower for case 2.a (51 W m^{-2}) than for the two other cases (244 and 279 W m^{-2}). Those heat source levels are in accordance with resulting cell temperatures. The same infrared radiative cooling is observed near the bottom boundary

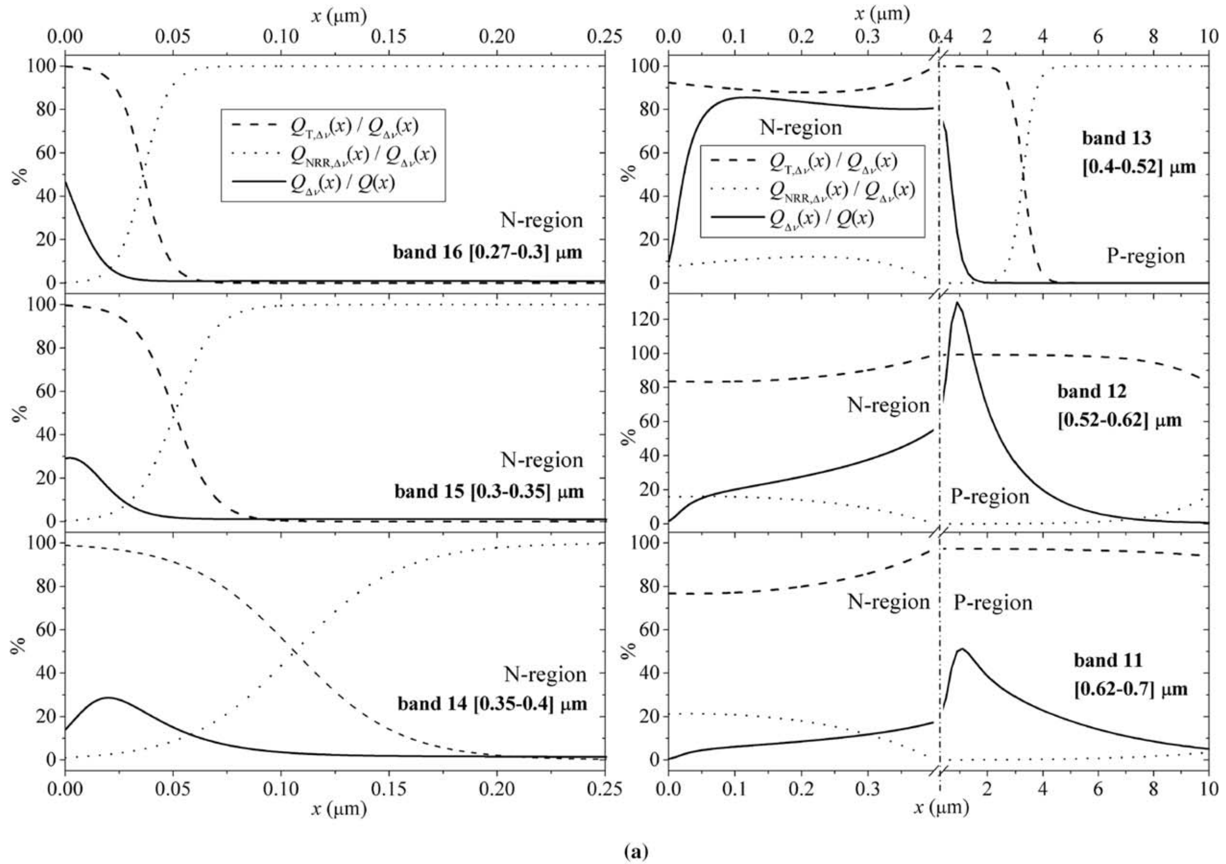

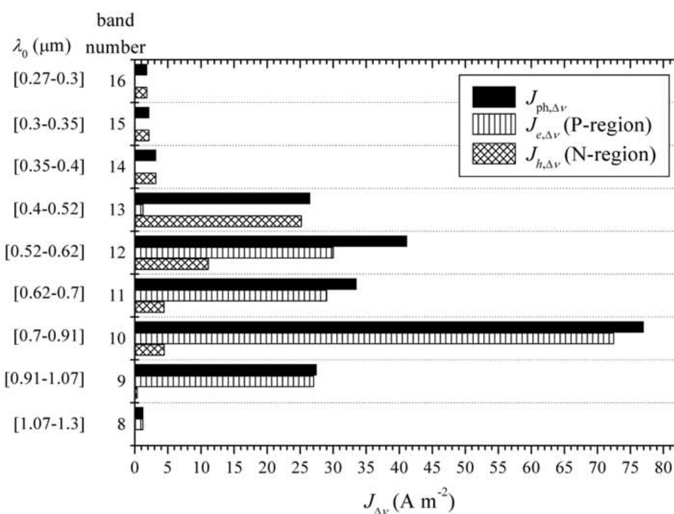

Fig. 7. (a) Spatial variations of heat sources ratios for spectral bands 11–16; (b) total, electron and hole current densities due to the photogeneration process for spectral bands 8–16.

($x \in [395, 400.4]$ μm). Then external infrared radiation sources play a notable role in the thermal behavior of the junction layer and have to be considered properly.

In any case, the total heat source is large near the top boundary which is subjected to solar irradiation. With respect to the spectral interband absorption coefficient (Fig. 3(a)), radiation with energy larger than the band gap is absorbed along the path from the surface and consequently carriers are non-homogeneously generated. For instance, solar radiation from bands 16, 15 and 14 ($\lambda_0 \in [0.27, 0.4]$ μm) is absorbed very near the surface (the absorption mean free path is less than 0.1 μm). Photogenerated minority carriers (holes in N-region) release their large excess energy by thermalization and since they are unlikely to reach the junction by diffusion, they also provide heat power through non-radiative recombination processes along the path. This is illustrated in Fig. 7(a), where ratios of the spectral heat source over the total heat source ($Q_{\Delta\nu}(x)/Q(x)$), of the spectral heat source due to the thermalization or to the non-radiative recombination processes over the spectral heat source ($Q_{T,\Delta\nu}(x)/Q_{\Delta\nu}(x)$ and $Q_{NRR,\Delta\nu}(x)/Q_{\Delta\nu}(x)$, respectively) are given as a function of distance for several spectral bands (for case 2.b). It is shown that the high level of the total heat source near the top boundary (Fig. 6) comes from the thermalization of carriers which have been generated through absorption of short wavelength radiation (bands 16, 15 and 14). Since that light is totally absorbed in the N-region, the photocurrent is only produced by holes diffusion (Fig. 7(b)). The same reasoning can be applied to spectral bands 13, 12 and 11 ($\lambda_0 \in [0.4, 0.7]$ μm, Fig. 7(a) and (b)). As a matter of fact, photon penetration depth tends to be larger so that some light reaches the P-region and the source of photocurrent is divided into hole (N-region) and electron (P-region) diffusion. As for local thermal sources, both thermalization and non-radiative recombination processes occur in the N-region. Electrons that are photogenerated in the P-region near the junction are mainly releasing their excess energy and are easily collected. This spectral analysis may be used for a larger investigation about the influence of many variables such as the junction properties (doping concentrations, surface recombination velocities, N and P region thicknesses, electron and hole diffusion lengths,...) on the coupled spectral radiation, thermal and carrier transport phenomena that take place in silicon photovoltaic cells.

Thermal boundary conditions (Table 3) essentially affect the cell equilibrium temperature (Table 4) as a function of the heat power generated within the whole layer (Eq. (17)) which itself mostly depends on the radiative boundary conditions and overall power balance. It has been shown that surroundings infrared irradiation is the cause of a substantial increase of the total internal heat power which leads to a cell temperature rise. This is observed for cases 1.a and 1.b (T_{cell} rises from 13.7 to 28.3 °C) as well as for cases 2.a and 2.b. (T_{cell} rises from 30.0 to 49.3 °C) for which thermal boundary conditions are identical (natural convection and same fluid temperature). As expected, considering that side 2 is thermally insulated causes a large cell temperature increase (case 1.d, $T_{cell} = 38.5$ °C). The most effective situation is encountered when temperature at side 2 of the cell is prescribed (case 1.c, $T_{cell} = 5.1$ °C), which is practically hard to achieve. As for case 2.c, when compared with case 2.b, thermal boundary conditions are modified by assuming an increase of both the heat exchange coefficient (5–10 W m^{-2} K^{-1}) and the fluid temperature (25–30 °C), which corresponds to a simplified representation of a transition from laminar to turbulent natural convection. It is found that the cell temperature slightly decreases from 49.3 to 46.9 °C.

From the above analysis, it is concluded that proper adjustment and control of both thermal and surroundings radiative boundary conditions are likely to provide guidelines for the improvement of photovoltaic cells performances.

5. Conclusion

In this paper, we have presented a physical and numerical modeling to evaluate photoelectric conversion performances of a c-silicon photovoltaic cell as a function of its temperature and taking into account thermal and irradiation operating conditions. The spectral radiative transfer problem is solved through a gray per band approach and a separated treatment of the collimated and diffuse components of radiation fluxes, by means, respectively, of a ray tracing method and a Composite Discrete Ordinates Method, that were previously developed [13]. The heat transfer modeling includes several local internal sources owing to thermal radiation, thermalization of carrier excess energy and carrier non-radiative recombinations. Continuity equations for excess minority carriers are solved for each spectral band considered for the radiative transfer problem and provide the current–voltage characteristic as well as local carrier densities required for the heat transfer equations. Required optical, radiative and thermophysical properties of c-silicon are determined by using existing databases and correlations. Once all solution methods have been detailed and validated against reference results separately for each phenomenon, specific features of the numerical technique employed to get a solution of the coupled problem have been given. In the application section, input parameters related to the junction layer properties, the radiative and thermal boundary conditions have been selected. The consistency of the numerical model has been demonstrated by checking the cell radiation balance and by evaluating the temperature dependence of electrical properties for several cases. Through a deeper analysis of the electrical and thermal behaviors as a function of thermal and radiative properties, it has also been shown that our model provides a lot of information which allow a sharp understanding of coupled phenomena and might be used for the derivation of an appropriate design and control of PV c-silicon cells. In future work, front and back glass covers and an antireflection coating will be added so as to

extend the model to standard photovoltaic modules. As an application, the resulting model will allow the complete study of the coupled spectral radiation–conduction–natural convection heat transfer problems together with the electrical efficiency determination for configurations of hybrid photovoltaic-thermal collectors used as vertical double-skin building facades [32].

References

[1] E. Radizemska, Thermal performance of Si and GaAs based solar cells and modules: a review, Prog. Energy Combust. Sci. 29 (2003) 407–424.

[2] T. Bergene, O.M. Løvvik, Model calculations on a flat plate solar heat collector with integrated solar cells, Sol. Energy 55 (6) (1995) 453–462.

[3] H.P. Garg, R.S. Adhikari, Transient simulation of conventional hybrid photovoltaic/thermal (PV/T) air heating collectors, Int. J. Energy Res. 22 (1998) 547–562.

[4] Y. Morita, T. Fujisawa, T. Tani, Moment performance of photovoltaic/thermal hybrid panel (numerical analysis and exergetic evaluation), Electr. Eng. Jpn. 133 (2) (2000) 43–51.

[5] M.W. Davis, A. Hunter Fanney, B.P. Dougherty, Prediction of building integrated photovoltaic cell temperatures, ASME J. Sol. Energy Eng. 123 (2001) 200–210.

[6] A.D. Jones, C.P. Underwood, A thermal model for photovoltaic systems, Sol. Energy 70 (4) (2001) 349–359.

[7] Y. Tripanagnostopoulos, TH. Nousia, M. Souliotis, P. Yianoulis, Hybrid photovoltaic/thermal solar systems, Sol. Energy 72 (3) (2002) 217–234.

[8] M.A. Green, Solar Cells Operating Principles Technology and System Applications, The University of New South Wales, Kensington, 1998.

[9] J.O. Schumacher, Numerical simulation of silicon solar cells with novel cell structures, Ph.D. thesis, Fraunhofer-Institut für Solare Energiesysteme, Freiburg, and Universität Konstanz, Germany, 2000.

[10] M.D. Dramincanin, Z.D. Rivtoski, P.M. Nikolic, D.G. Vasiljevic, D.M. Todorovic, Photoacoustic investigation of transport in semiconductors: theoretical and experimental study of a Ge single crystal, Phys. Rev. B 51 (20) (1995) 14226–14232.

[11] I. Reich, M.L. Gomez-Herrera, P. Diaz, J.G. Mendoza-Alvarez, J.L. Herrera-Perez, E. Marin, Measurement of the Auger lifetime in GaInAsSb/GaSb heterostructures using the photoacoustic technique, Appl. Phys. Lett. 79 (7) (2001) 964–966.

[12] D.H. Macdonald, Recombination and trapping in multicrystalline silicon solar cells, Ph.D. thesis, The Australian National University, Canberra, Australia, 2001.

[13] C. Muresan, R. Vaillon, C. Ménézo, R. Morlot, Discrete ordinates solution of coupled conductive radiative heat transfer in a two-layer slab with Fresnel interfaces subject to diffuse and obliquely collimated irradiation, J. Quant. Spectrosc. Radiat. Transfer 84 (2004) 551–562.

[14] K. Rajkanan, R. Sing, J. Shewchun, Absorption coefficient for solar cell calculations, Solid-State Electron. 22 (1979) 793–795.

[15] R. Hull, Properties of crystalline silicon, EMIS Datareviews Series No. 20, INSPEC, The Institution of Electrical Engineers, London, 1999.

[16] V. Alex, S. Finkbeiner, J. Weber, Temperature dependence of the indirect energy gap in crystalline silicon, J. Appl. Phys. 79 (9) (1996) 6943–6946.

[17] M.A. Green, M.J. Keevers, Optical properties of intrinsic silicon at 300 K, Prog. Photovoltaics: Res. Appl. 3 (1995) 189–192.

[18] D.A. Clugston, P.A. Basore, Modelling free-carrier absorption in solar cells, Prog. Photovoltaics: Res. Appl. 5 (1997) 229–236.

[19] R.J. Collins, H.Y. Fan, Infrared lattice absorption bands in germanium, silicon and diamond, Phys. Rev. 93 (4) (1953) 674–678.

[20] C.J. Glassbrenner, G.A. Slack, Thermal conductivity of silicon and germanium from 3 K to the melting point, Phys. Rev. 134 (4A) (1964) A1058–A1069.

[21] G.A. Slack, Thermal conductivity of pure and impure silicon carbide and diamond, J. Appl. Phys. 35 (12) (1964) 3460–3466.

[22] C. Leroy, P. Roy, G.L. Casse, M. Glaser, E. Grigoriev, F. Lemeilleur, Charge transport in nonirradiated and irradiated silicon detectors, Nucl. Instrum. Meth. Phys. Res. A 434 (1999) 90–102.

[23] M.T. Heath, Scientific Computing an Introductory Survey, second ed., McGraw-Hill, New York, 2002.

[24] C.M. Spuckler, R. Siegel, Refractive index and scattering effects on radiation in a semi-transparent laminated layer, J. Thermophys. Heat Transfer 8 (2) (1994) 193–201.

[25] M.F. Modest, Oblique collimated irradiation of an absorbing, scattering, plane–parallel layer, J. Quant. Spectrosc. Radiat. Transfer 45 (5) (1991) 309–312.

[26] C. Proulx, D.R. Rousse, R. Vaillon, J.-F. Sacadura, Handling of collimated irradiation on a plane–parallel participating medium, Proc. ASME Heat Transfer Div. 336 (1) (2000) 85–92.

[27] B.T. Liou, C.Y. Wu, Composite discrete-ordinate solutions for radiative transfer in a two-layer medium with Fresnel interfaces, Numer. Heat Transfer Part A 30 (1996) 739–751.

[28] M.F. Modest, Radiative Heat Transfer, first ed., McGraw-Hill, New York, 1993.

[29] R. Siegel, J.R. Howell, Thermal Radiation Heat Transfer, third ed., Taylor & Francis, Washington, 1992.

[30] D.R. Myers, K. Emery, C. Gueymard, Revising and validating spectral irradiance reference standards for photovoltaic performance evaluation, J. Sol. Energy Eng. 126 (2004) 567–574.

[31] R.E. Bird, C. Riordan, Simple solar spectral model for direct and diffuse irradiance on horizontal and tilted planes at the earth's surface for cloudless atmospheres, J. Appl. Meteorol. 25 (1) (1986) 87–97.

[32] C. Muresan, C. Ménézo, R. Bennacer, R. Vaillon, Numerical simulation of a vertical solar collector integrated in building frame: radiation and turbulent natural convection coupling, Heat Transfer Eng. 27 (2) (2006) 29–42.